

**Photodissociation dynamics of jet-cooled H<sub>2</sub>O and D<sub>2</sub>O in the non-Franck–Condon regime: Relative absorption cross sections and product state distributions at 193 nm**

David F. Plusquellic, Ondrej Votava, and David J. Nesbitt

Citation: *The Journal of Chemical Physics* **107**, 6123 (1997); doi: 10.1063/1.474280

View online: <http://dx.doi.org/10.1063/1.474280>

View Table of Contents: <http://scitation.aip.org/content/aip/journal/jcp/107/16?ver=pdfcov>

Published by the [AIP Publishing](#)

---

**Articles you may be interested in**

The complex spectrum of a “simple” free radical: The  $\tilde{A} - \tilde{X}$  band system of the jet-cooled boron difluoride free radical

*J. Chem. Phys.* **135**, 094305 (2011); 10.1063/1.3624528

Determination of the excited-state structure of 7-azaindole-water cluster using a Franck-Condon analysis

*J. Chem. Phys.* **123**, 224311 (2005); 10.1063/1.2136868

Ab initio potential energy surfaces, total absorption cross sections, and product quantum state distributions for the low-lying electronic states of N<sub>2</sub>O

*J. Chem. Phys.* **122**, 054305 (2005); 10.1063/1.1830436

Bond-selective photofragmentation of jet-cooled HOD at 193 nm: Vibrationally mediated photochemistry with zero-point excitation

*J. Chem. Phys.* **109**, 6631 (1998); 10.1063/1.477314

The state-to-state photodissociation dynamics of HOD ( $\tilde{A}$ )

*J. Chem. Phys.* **106**, 6354 (1997); 10.1063/1.473625

---



# Photodissociation dynamics of jet-cooled H<sub>2</sub>O and D<sub>2</sub>O in the non-Franck–Condon regime: Relative absorption cross sections and product state distributions at 193 nm

David F. Plusquellic,<sup>a)</sup> Ondrej Votava,<sup>a)</sup> and David J. Nesbitt<sup>b)</sup>  
*JILA, National Institute of Standards and Technology and University of Colorado, and Department of Chemistry and Biochemistry, University of Colorado, Boulder, Colorado 80309-0440*

(Received 9 May 1997; accepted 21 July 1997)

Quantum state distributions for nascent OH and OD fragments generated by Franck–Condon “forbidden” 193 nm photodissociation of H<sub>2</sub>O and D<sub>2</sub>O are reported, with the two isotopomers initially prepared in their zero-point vibrational and lowest ortho/para nuclear spin allowed rotational states (i.e.,  $J_{K_a K_c} = 1_{01}$  and  $0_{00}$  in a 3:1 ratio for H<sub>2</sub>O and 1:2 ratio for D<sub>2</sub>O) by cooling in a slit supersonic expansion. Product state distributions are probed via OH/OD laser-induced fluorescence (LIF) with cylindrical mirror collection optics optimized for the slit expansion geometry, which makes photodissociation studies feasible with cross sections as low as  $\approx 10^{-26}$  cm<sup>2</sup>. The OH and OD fragments are formed exclusively in  $v = 0$ , but with highly structured quantum state distributions in rotational,  $\Lambda$ -doublet, and fine structure levels ( $^2\Pi_{3/2}^+$ ,  $^2\Pi_{1/2}^+$ , and  $^2\Pi_{3/2}^-$ ) that exhibit qualitatively different trends than observed in previous jet photolysis studies at 157 nm in the Franck–Condon “allowed” regime. The relative OH/OD fragment yields at 193 nm indicate a  $64 \pm 10$  times greater propensity for OH vs OD bond cleavage in H<sub>2</sub>O than D<sub>2</sub>O, which is more than three-fold smaller than predicted from full three-dimensional quantum scattering calculations on ground ( $\tilde{X}^1A_1$ ) and first excited state ( $\tilde{A}^1B_1$ ) potential surfaces. One-dimensional semiclassical calculations of the Franck–Condon overlap matrix elements confirm these discrepancies to be considerably outside uncertainties associated with the ground and excited state potential surfaces. These results indicate that the photodissociation dynamics for this benchmark system are not yet fully understood and suggest either non-Born–Oppenheimer effects or contributions from other electronic surfaces may be important in the extreme non-Franck–Condon photolysis regime. © 1997 American Institute of Physics. [S0021-9606(97)02940-1]

## I. INTRODUCTION

The photodissociation dynamics of H<sub>2</sub>O in the first absorption band has been the target of numerous experimental studies aimed at probing the detailed dependence of the OH photofragment distributions on (i) the character of the initially prepared rovibrational state and (ii) energy of the dissociating photon. Closely paralleling these experimental efforts, intensive theoretical calculations have been performed using both classical trajectory<sup>1</sup> and quantum mechanical scattering methods<sup>2,3</sup> on *ab initio* and semiempirical potential energy surfaces (PES). As demonstrated in these combined studies, a truly remarkable level of agreement exists between experiment and theory, both for dissociation studies of the  $|00\rangle^+$  ground state in the classical Franck–Condon regime at 157 nm<sup>4</sup> as well as the vibrationally mediated photolysis (VMP) studies<sup>5–8</sup> of selectively excited  $|01\rangle^-$ ,  $|04\rangle^-$ , and  $|05\rangle^-$  levels of H<sub>2</sub>O. For clarity and consistency with the literature, the vibrational notation throughout this paper will follow that of Child and co-workers;<sup>9</sup> specifically,

$|v_1, v_3\rangle^\pm$  labels will be used to designate vibrations that correspond to symmetric and antisymmetric combinations of local mode OH/OD stretches.

One of the earliest demonstrations of this excellent agreement was obtained from time-independent quantum scattering calculations of H<sub>2</sub>O and D<sub>2</sub>O photolysis cross sections by Schinke and co-workers,<sup>10,11</sup> and later by Imre and co-workers<sup>3</sup> with time-dependent methods. Particularly when the thermal distribution over initial  $J_{K_a K_c}$  states is included, the VUV absorption cross sections for H<sub>2</sub>O and D<sub>2</sub>O between 155 and 190 nm are in near quantitative agreement with the observed spectra.<sup>12</sup> Since then, OH distributions from the absorption of room temperature and jet-cooled H<sub>2</sub>O at 193 nm have been reported by Comes and co-workers,<sup>13</sup> and at about the same time by Häusler *et al.*<sup>5</sup> in VMP studies of  $|01\rangle^- 0_{00}$  H<sub>2</sub>O, where direct 193 nm photodissociation was found to contribute weak OH background signals. The weakness of such signals is readily appreciated; vertical transitions at 193 nm require excitation far into the classically “forbidden” regions of the OH stretch potential, where the ground state wave function amplitude is rapidly decaying and absorption cross sections can be down by 10<sup>5</sup> or more. Due to additional exponential attenuation of the vibrational wave functions, two to three orders of magnitude smaller absorbances are anticipated for D<sub>2</sub>O vs H<sub>2</sub>O, in essence, an enormous “isotope effect” is predicted in the UV absorption

<sup>a)</sup>Current address: Optical Technology Division, National Institute of Standards and Technology, Gaithersburg, MD.

<sup>b)</sup>Staff member, Quantum Physics Division, National Institute of Standards and Technology.

cross sections. Consistent with these expectations, there have been no previous photolysis studies of D<sub>2</sub>O at wavelengths greater than 180 nm. However, as we attempt to elucidate in this paper, it is precisely this additional sensitivity in the ‘‘extreme non-Franck–Condon’’ regime that makes possible the most demanding tests of the photodissociation dynamics.

These studies and others have sparked a renewed interest in the photodissociation dynamics of supersonically cooled H<sub>2</sub>O and D<sub>2</sub>O at 193 nm for a variety of reasons. First of all, it is thought that only at the onset of the absorption spectrum where the bound and continuum wave functions begin to overlap are simple pictures of partial cross sections into the individual product channels valid.<sup>14</sup> Thus, wave packet dynamics initiated from these regions should be intrinsically much simpler to interpret and less sensitive to errors introduced by approximate methods. Second, by supersonically cooling into the lowest rotational levels of H<sub>2</sub>O and D<sub>2</sub>O, one can obtain quantum state specific information with which to test the predicted dynamics without averaging over thermally excited states. Third, absorption at 193 nm occurs far to the red of the absorption peak maximum at 165 nm, sampling the wave function well beyond the outer turning points on the ground potential energy surface. Isotope data in this regime is exponentially sensitive to the photodissociation dynamics and provide the most stringent tests of potential energy surfaces and the underlying photolysis models. Finally, photodissociation dynamics in the extreme non-Franck–Condon regime necessarily plays an important role in the quantum state selectivity of IR+UV double resonance schemes.<sup>5,6,15</sup> Indeed, the stimulus for the present study of isotope effects in photolysis of H<sub>2</sub>O developed out of ongoing efforts in vibrationally mediated photolysis in H<sub>2</sub>O and HOD containing clusters.<sup>15–17</sup>

A simplified explanation for the large isotope effects anticipated for H<sub>2</sub>O/D<sub>2</sub>O photolysis is demonstrated in Fig. 1. Here, the ground state ( $\tilde{X}^1A_1$ ) PES (dashed lines) is taken from the work of Sorbie and Murrell<sup>18</sup> (SM) and shown as a function of the two OH stretch coordinates at a fixed bond angle of 104.5°. Superimposed on this surface are two-dimensional (2D) contour plots (solid lines) of the square moduli of the ground state wave functions of H<sub>2</sub>O (top) and D<sub>2</sub>O (bottom). Also shown with shaded regions are cuts on the *ab initio* first excited state ( $\tilde{A}^1B_1$ ) PES of Staemmler and Palma<sup>11,19</sup> (SP) that correspond to vertically accessible regions at wavelengths  $\geq 193$  nm relative to the zero-point vibrational energies.

Along these 193 nm cuts corresponding to the conservation of energy, the probability density for both H<sub>2</sub>O and D<sub>2</sub>O state wave functions is quite small, which accounts for the extremely low UV cross sections observed in the present study ( $\approx 10^{-23}$ – $10^{-25}$  cm<sup>2</sup>). The exponential decrease with increasing bond length is especially prominent in D<sub>2</sub>O, whose reduced zero-point energy forces the absorption at 193 nm to extend farther out in the tail of the OD stretch wave function. In both cases, the greatest absorption probability occurs in very narrow regions localized near the innermost point of intersection of the upper  $^1B_1$  surface and

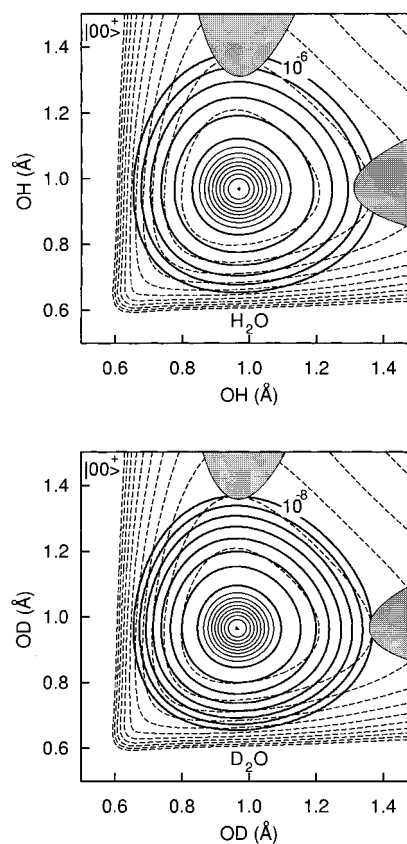


FIG. 1. Two-dimensional contour plot of the Sorbie–Murrell ground state potential energy surface at a fixed 104.5° bond angle (dashed lines at 1 eV spacing) and wave function square modulus (solid lines) for H<sub>2</sub>O (top) and D<sub>2</sub>O (bottom) along the two stretch coordinates. Also shown are shaded regions on the Staemmler and Palma excited state PES (Ref. 19) energetically accessible at 193 nm; the extremely low probability amplitudes illustrate the far off-resonance absorption behavior. The inner contours decrease linearly from a peak value of 1 in 0.1 unit intervals; the heavier lines mark tenfold sequential decreases.

the ground state wave function tail. Since the Franck–Condon absorption is dominated by  $|\Psi|^2$  near these inner turning points, the ratio of 193 nm absorption cross sections,  $\sigma_{\text{H}_2\text{O}}/\sigma_{\text{D}_2\text{O}}$ , is anticipated from the corresponding probability densities to be of order  $10^2:1$ – $10^3:1$ . Though based on a simplified picture, this estimate is in good qualitative agreement with more rigorous predictions of  $>200:1$  by Schinke and co-workers<sup>20</sup> from full quantum scattering calculations on these surfaces. As we demonstrate in this paper, the experimentally observed isotope effect is significantly smaller than these predictions and cannot be accounted for by uncertainties in the ground and excited state potential surfaces. Thus, in contrast to the excellent agreement in the classically Franck–Condon ‘‘allowed’’ regime, these results indicate that photodissociation dynamics of H<sub>2</sub>O and D<sub>2</sub>O in the Franck–Condon ‘‘forbidden’’ regime are not satisfactorily understood by current theoretical models.

The rest of this paper is organized as follows. A description of the experimental apparatus is given in Sec. II, followed by a discussion in Sec. III of isotopic sample purity and accommodation in the gas delivery system. Diagnostic

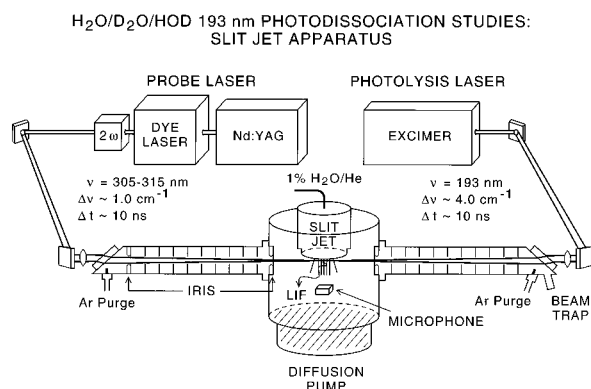


FIG. 2. Schematic of the slit-jet photofragmentation apparatus. Fluorescence is collected at right angles to the jet expansion axis and counterpropagating photolysis/probe beams.

tests are presented in Sec. IV, with attention given to methods used to extract populations from the integrated transition intensities. The internal state distributions in the  $\Pi_{3/2}^+$ ,  $\Pi_{1/2}^+$ , and  $\Pi_{3/2}^-$  fine structure levels of OH and OD are presented in Sec. V and, from sums over these distributions, the relative 193 nm UV absorption cross section of H<sub>2</sub>O and D<sub>2</sub>O. Trends in the rotational,  $\Lambda$ -doublet and spin state distributions from 193 nm off-resonance photolysis are discussed and compared with those obtained from on-resonance studies at 157 nm.<sup>4</sup> In the Sec. VI, the sensitivity of these predictions to uncertainties in the potential energy surfaces is examined via WKB semiclassical modeling of the photolysis cross section ratios, which does not account for the present discrepancy between theory and experiment. Finally, we speculate on possible reasons for these discrepancies and indicate directions for further theoretical effort. In particular, this work raises the intriguing possibility of competitive photodissociation from the excited *triplet* surface ( $\tilde{a}^3B_1$ ), which is theoretically addressed elsewhere<sup>20</sup> by Schinke and co-workers.

## II. EXPERIMENT

A schematic of the experimental arrangement used in the photodissociation studies of H<sub>2</sub>O and D<sub>2</sub>O is illustrated in Fig. 2. The vacuum chamber consists of two 40 cm long baffle arms, a 4 cm × 50 μm slit jet<sup>21</sup> and a light collection assembly. The photolysis and probe light pulses counter-propagate through the baffle arms into the 4 cm gas expansion region of the slit jet, 1.27 cm downstream of the nozzle. The light collection assembly (Fig. 3) is positioned at right angles to both the expanding gas and the propagation direction of the lasers. Mounted on the end of each baffle arm is a 10 mm fused silica window set at Brewster's angle with respect to the probe laser polarization and two externally adjustable irises in order to minimize the light scattered along the beam path from reaching the detector. One iris in each arm is located just after the Brewster window and one just before the light collection assembly. A beam trap is positioned at the exit window to prevent backscattering of reflected light from the exit window. Additionally, microjets

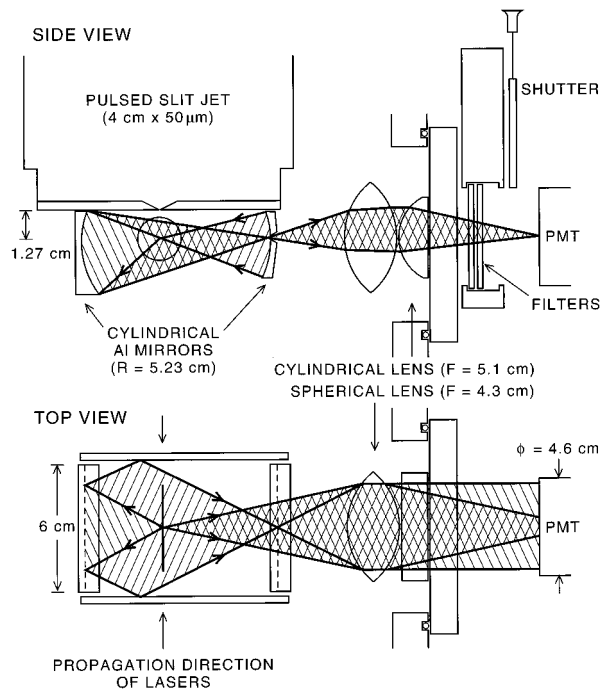


FIG. 3. Light collection assembly optimized for the slit-jet geometry showing cross sectional views from the side (upper panel) and the top (lower panel). The system images a  $\phi$  1 mm × 40 mm column of fluorescence 1.27 cm downstream of the nozzle onto the PMT with  $\sim 5\%$  efficiency. Rejection of scattered laser light is measured to be  $> 10^9$  (see the text for details).

purge the surface of the window and the baffle arms with a continuous stream of Ar gas to prevent buildup of diffusion pump oil photolysis residue.

The photolysis laser is an excimer operating with ArF unstable resonator optics at 193 nm ( $\Delta\nu \sim 30$  cm<sup>-1</sup>). The output beam is reduced from 1 × 2.5 cm to 1 cm<sup>2</sup> with a cylindrical condenser lens and mildly focused into a  $\phi_D \sim 1.0$  mm beam through the slit jet region with a  $f = 1.0$  m fused silica lens. The pulse energies in the interaction region are typically  $\sim 1$  mJ/mm<sup>2</sup>/pulse. The laser is unpolarized except for  $s$ -reflective losses from the two turning mirrors and the Brewster entrance window. The probe laser is an Nd:YAG pumped dye laser operating with DCM/R640 dye mix whose output is frequency doubled for LIF detection of OH and OD on the  $\tilde{A}^2\Sigma^+(v'=0) - \tilde{X}^2\Pi(v''=0)$  transitions near 308 nm.<sup>22</sup> The UV beam is separated from the fundamental using dichroic optics and focused at the slit jet to a  $\phi_D \sim 0.4$  mm beam. The probe laser is vertically polarized in a plane perpendicular to the detection axis and has an instrumental linewidth of about 1.5 cm<sup>-1</sup>.

What makes these far off-resonance photolysis studies feasible is the high number density and pathlength advantages of a pulsed slit supersonic expansion,<sup>21</sup> which when coupled with low background LIF techniques, currently permits detection of absorption cross sections down to  $\lesssim 10^{-26}$  cm<sup>2</sup>. The slit geometry light collection assembly for LIF detection of OH and OD is shown in Fig. 3 and is es-

essentially the cylindrical analog of the spherical design optimized for pinhole expansions by Majewski *et al.*<sup>23</sup> The upper panel of Fig. 3 shows the assembly as viewed from the side with the long dimension of the slit jet perpendicular to the page. Front and rear UV enhanced aluminum coated cylindrical mirrors (5.23 cm radius of curvature) image a  $\phi_D$  1.4 mm  $\times$  60 mm cylindrical section at the crossing of the jet and laser beams through a 1  $\times$  60 mm slit in the rear mirror. The lower section of Fig. 3 illustrates the top view of this system. Two planar and parallel mirrors are positioned on opposite sides of the cylindrical mirrors to improve scattered light rejection and enhance the collection efficiency. Each mirror has a 1.27 cm hole centered at the interaction region so that the excimer and UV probe lasers pass unobstructed. The condenser assembly consists of one biconvex spherical ( $f=5.1$  cm) and one plano-convex cylindrical ( $f=4.3$  cm) CaF<sub>2</sub> lens that effectively reduce the image size from 1  $\times$  40 mm at the crossing to 1 mm  $\times$  10 mm at the  $\phi_D = 46$  mm PMT. A 5.0 cm square filter assembly in front of the PMT houses two dielectric coated notch filters, each having  $R > 99.5\%$  reflectivity at 193 nm and  $> 90\%$  transmissivity from 250–400 nm. These notch filters reflect stray excimer light and thus eliminate problems typically encountered with bulk absorption filters from fluorescence emitted at longer wavelengths.

The degree of spatial filtering and fluorescence collection efficiency of the imaging system are measured using 10  $\mu$ J of the probe laser. With the chamber pressure below  $10^{-5}$  Torr, (1 Torr =  $1.333 \times 10^{-3}$  bar), the measured ratio of scattered photons detected by the PMT to the total number per pulse is less than  $10^{-9}$ . The detection efficiency is determined in a Rayleigh scattering experiment using  $\sim 30$  Torr of Ar gas,<sup>24</sup> from which the fraction of photons collected is estimated to be 5% over the 4 cm slit length. This is somewhat less than expected from geometric considerations, but as much as an order of magnitude larger than for conventional point source imaging. A four-channel digital pulse generator triggers the pulsed valve, excimer, and the Q switch of the probe laser with an accuracy and jitter of better than 1 ns. The timing of the excimer and probe lasers are set to sample near the center of the gas pulse, the probe laser firing about 200 ns after the excimer. The PMT signal is sampled with a gated integrator and boxcar averager. The gate width and delay are set to sample the 300 ns window directly following the probe laser pulse.

A microphone positioned 4 cm downstream of the slit jet monitors the gas pulse shape (500  $\mu$ s) and stability on a shot-to-shot basis; this signal is proportional to the LIF intensity and backing pressure to better than 5% and is used to normalize the LIF signals to the beam density in the interaction region. The valve is heated to  $\sim 30$  °C in order to prevent condensation of the premixed gas samples of 1% H<sub>2</sub>O (D<sub>2</sub>O) in He buffer gas diluent. In switching between H<sub>2</sub>O and D<sub>2</sub>O, multiple purge cycles are performed and monitored for the OH/OD ratio in the photolysis region until complete isotopic passivation of surfaces is achieved. The chamber is pumped with a 6 in. diffusion pump and a two-stage rough pump. With no gas load, the base pressure of the sys-

tem is in the  $10^{-6}$  Torr range. With the window purge system operating, a steady background pressure of  $10^{-4}$  Torr is maintained. With the pulsed jet operating at 10 Hz and at stagnation pressures less than 760 Torr, the chamber pressure is less than  $10^{-3}$  Torr.

The single shot output of the boxcar averager is sampled directly with a 12-bit analog-to-digital converter (A/D). Split off portions of the probe and excimer laser energies are monitored with a photodiode and pyroelectric detector, respectively. These laser pulse energy signals, as well as the microphone signal monitoring the gas pulse density, are captured by an analog gated sample and hold circuits and are then read by independent A/Ds interfaced with the data acquisition computer. Finally, dye laser fringes from a thin plate etalon (FSR =  $3$  cm<sup>-1</sup>) are recorded to provide a linear frequency calibration of the OH and OD spectra. All data are saved to disk in order to correct for pump and probe laser energy fluctuations on a shot-to-shot basis.

### III. ISOTOPIC PURITY AND SAMPLE PREPARATION

Since OD fragments can be formed by photolysis of both HOD or D<sub>2</sub>O, isotopic purity for both sample and gas delivery systems must be well characterized. D<sub>2</sub>O is purchased commercially; the quoted sample purity of 99.8% is quantitatively confirmed by NMR. Additional tests to determine the extent of accommodation of the gas delivery system to the complete exchange of the different isotopes are performed as follows. An evacuated gas holding tank is filled to 17 Torr directly from vapor over the D<sub>2</sub>O liquid sample and then pumped out to  $< 100$  mTorr; this procedure is repeated many times to ensure the isotopic composition of the gas in the delivery system is equivalent to the liquid sample purity. To verify that the slit pulsed valve assembly is also fully passivated in a similar series of pump-fill cycles, a 1% dilution of the gas mix in He is expanded and photolyzed at 193 nm, which allows the spectral regions near the  $Q_1(1)$  lines of OH and OD to be recorded. As determined from the OH and OD integrated intensities, the percentages of HOD in the gas mix decrease systematically with the number of pump-fill exchange cycles from 1.3%:1.0%:0.5%:0.4%. After the fourth exchange, the isotopic purity of the gas samples is  $> 99.5\%$ , which is maintained for all gas samples used in this study. As described in accompanying studies<sup>25</sup> of OH/OD photolysis branching ratios for HOD, we have measured the OD (and OH) yields for various gas mixtures containing up to 50% HOD and find that the percent HOD composition necessary to *double* the OD signal from photolysis of both D<sub>2</sub>O and the O–H bond in HOD is 5%. Thus, the ten-fold smaller ( $< 0.5\%$ ) HOD impurity makes only a minor contribution to the D<sub>2</sub>O photolysis data and is explicitly corrected for in the determination of the relative absorption cross sections.

Initial states of H<sub>2</sub>O and D<sub>2</sub>O monomers are prepared by supersonic expansion of 1% mixtures in He through a slit jet. Stagnation pressures are maintained near 340 Torr, where a possible contribution from the photodissociation of clusters is negligible; tests demonstrate a linear LIF signal depen-

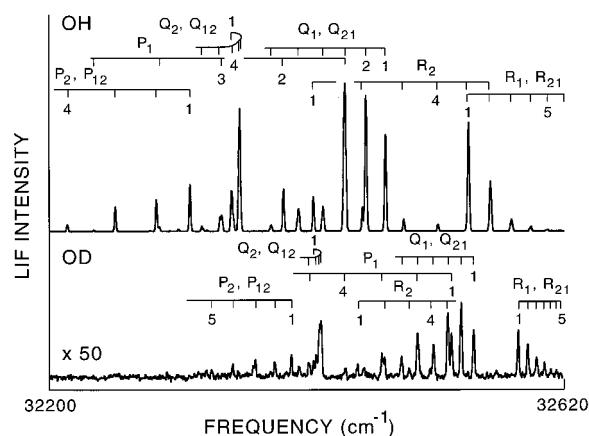


FIG. 4. LIF spectra of OH ( $v=0$ ) and OD ( $v=0$ ), obtained from 193 nm photodissociation of jet-cooled H<sub>2</sub>O and D<sub>2</sub>O. The OD intensities are multiplied by factor of 50.

dence on stagnation pressure for all experimental conditions sampled (100–500 Torr). Based on extensive direct IR laser absorption studies in our laboratories under these stagnation conditions, the rotational temperature in the slit jet<sup>26</sup> is estimated to be 5–10 K, which is sufficient to cool the monomers completely into the lowest allowed ortho/para nuclear spin states. Thus, the product state distributions reflect photodissociation of these isotopomers from the  $J_{K_a K_c} = 0_{00}$  and  $1_{01}$  rotational levels, appropriately weighted by 1:3 or 2:1 for H<sub>2</sub>O and D<sub>2</sub>O, respectively.

#### IV. DIAGNOSTICS FOR DETERMINING OH AND OD STATE POPULATIONS

Sample data for the LIF excitation spectra of OH and OD following 193 nm photolysis of jet-cooled H<sub>2</sub>O and D<sub>2</sub>O are shown in Fig. 4, where the quantum state labels for the transitions are those of Dieke and Crosswhite.<sup>27</sup> The quantum number  $N$  designates the total angular momentum without electron spin ( $S$ ) with the total angular momentum ( $J = N + S$ ) quantum number,  $J = N + 1/2$  and  $N - 1/2$ , for the  $\Pi_{3/2}$  and  $\Pi_{1/2}$  ground states, respectively.  $P$ ,  $Q$ , and  $R$  transitions specifically refer to changes in  $N$ , with subscripts 1 and 2 designating the  $\Pi_{3/2}^{+/-}$  and  $\Pi_{1/2}^{+/-}$  spin orbit states, respectively.  $Q$  lines probe the  $\Pi^-$   $\Lambda$ -doublet components and  $P/R$  transitions probe the  $\Pi^+$   $\Lambda$ -doublet component,<sup>4,27,28</sup> which, in principle, allows all four lower sublevels to be probed independently. However, due to strong overlap in the  $Q$  branch lines accessing the  $\Pi_{1/2}$  manifold at our probe laser resolution, only the  $\Pi_{3/2}^+$ ,  $\Pi_{3/2}^-$ , and  $\Pi_{1/2}^+$  populations can be reliably obtained from the data.

The absence of multiphoton processes in the UV photolysis step can be easily verified by power-dependent studies. LIF excitation spectra of OH/OD are obtained by photolyzing jet-cooled H<sub>2</sub>O/D<sub>2</sub>O samples over the range of excimer pulse energies from 0 to 10 mJ. The fluorescence intensities of R<sub>1</sub> branch transitions in OH and OD are then integrated and plotted as a function of excimer energy for H<sub>2</sub>O (top) and D<sub>2</sub>O (bottom), along with the best fit lines

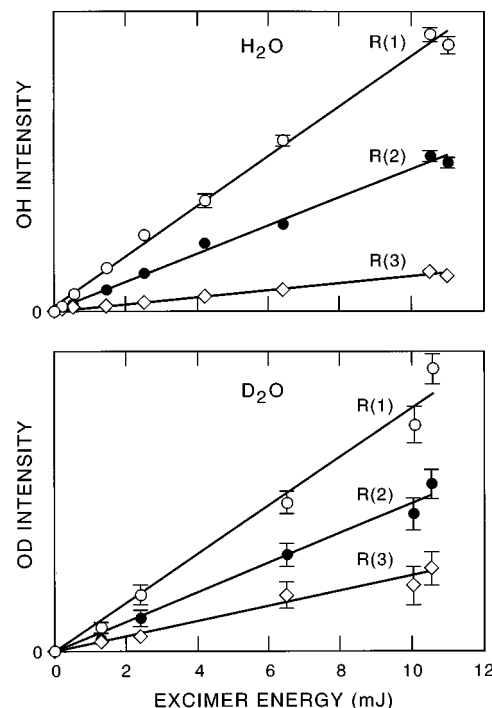


FIG. 5. The integrated signal intensity dependence on excimer pulse energy for OH (top) and OD (bottom). The linear behavior verifies that only single photon absorption processes are contributing.

through these data. As shown in Fig. 5, no deviation from a linear signal dependence is observed up to the highest pulse energies tested.

The probe laser operates typically at pulse energies between 10–20  $\mu\text{J}$  ( $\Delta t \approx 7$  ns,  $\Delta \nu \approx 1$   $\text{cm}^{-1}$  beam diameter  $\approx 0.4$  mm) corresponding to LIF detection in a predominantly linear regime.<sup>29,30</sup> In the linear limit, the population,  $n(v'', J'')$ , in a specific rovibrational state of OH (or OD) is proportional to the integrated line intensity,  $S$ , given by

$$S \propto B \cdot n(v'', J'') \cdot I_{\text{probe}}, \quad (1)$$

where  $B$  is the Einstein coefficient for absorption<sup>29</sup> and  $I_{\text{probe}}$  is the probe laser pulse energy. To rigorously correct for effects from partial saturation, the LIF signal dependence on probe laser power is measured independently for all OH and OD transitions used in the population analysis. OH and OD spectra are recorded at pump-probe delays of 5  $\mu\text{s}$  on gas samples in a static cell containing 1.5% H<sub>2</sub>O and D<sub>2</sub>O in 50 Torr of He. Under these conditions, greater than 20 gas kinetic collisions have occurred, and thus the rotational state distributions are completely thermalized to 300 K. This is experimentally confirmed by monitoring the rotational distributions as a function of time delay; no change in the relative intensities is observed upon increasing the delay by an additional factor of 3. The R branch integrated intensities are shown in Fig. 6 for probe energies from 0.04 up through 70

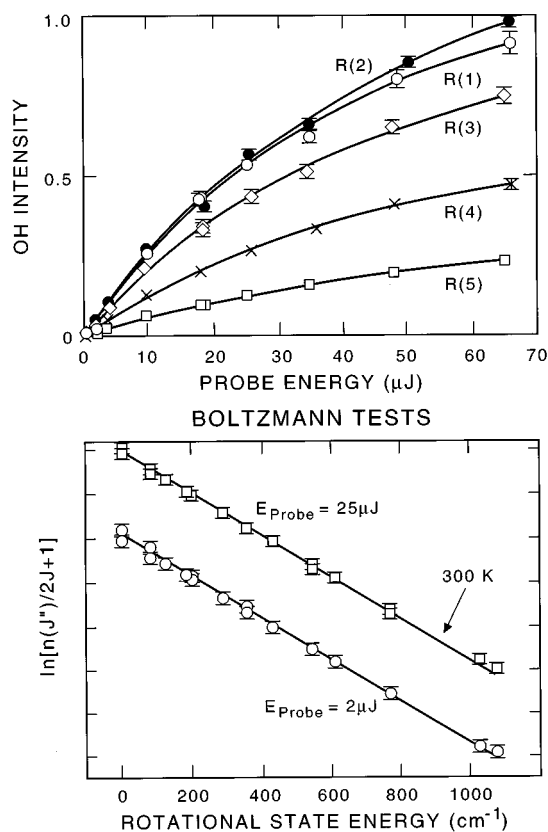


FIG. 6. Saturation behavior of the integrated LIF intensities of R<sub>1</sub> and R<sub>21</sub> rotational lines of OH as a function of the probe laser energy. The populations determined using Eq. (2) and Table I are shown in a Boltzmann plot (bottom) for spectra measured at 2 μJ (lower trace) and 25 μJ (upper trace) of probe energy. The straight lines represent the expected 300 K distribution.

μJ. As evident at energies greater than ~10 μJ, the onset of saturation begins where signals clearly deviate from the linear dependence observed at the lower probe energies.

We fit the saturation behavior to a standard expression,<sup>31</sup>

$$S \propto B \cdot n(v'', J'') \cdot I_{\text{probe}} \cdot m_1 / (1 + m_2 \cdot I_{\text{probe}}), \quad (2)$$

where the Einstein B coefficient is taken from the Kinsey database<sup>29</sup> and  $m_1$  and  $m_2$  are parameters fit to these data. In the linear signal limit ( $I_{\text{probe}} \leq 10 \mu\text{J}$ ), the integrated intensities for all lines are first normalized to their Boltzmann populations and plotted as a function of the Einstein B coefficient to extract  $m_1$ . For fixed  $m_1$ , the  $m_2$  parameters are then fit to the data over the full range of pulse energies for each rovibrational line. The model predictions are shown with heavy lines in Fig. 6 and a summary of these parameters is given in Table I. The  $m_2$  values within a given branch vary by less

TABLE I. Probe laser calibration factors used to model the saturation behavior of OH and OD (see the text for details).

	R <sub>1</sub> and R <sub>21</sub>	R <sub>2</sub>	P <sub>1</sub>	P <sub>2</sub> and P <sub>12</sub>	Q <sub>1</sub> and Q <sub>21</sub>
$m_1$	1.0	0.952	0.760	0.820	0.667
$m_2$	0.018	0.018	0.025	0.024	0.026

than 25% and are reported in Table I as an average over all rotational lines.

As an explicit test of this procedure, the lower part of Fig. 6 illustrates a Boltzmann plot of the populations determined from Eq. (2) for an equilibrated room temperature OH sample. The upper and lower curves correspond to 2 and 25 μJ of probe pulse energy, respectively. The straight lines through each dataset correspond to the expected 300 K Boltzmann distribution with ±10% error bars. Furthermore, the populations derived from relative intensities of P/R branch pairs for the jet-cooled samples agree to within 10%. As a final test, the same saturation parameters in Table I for OH also correctly reproduce the saturation behavior experimentally observed for OD.

## V. RESULTS

### A. OH and OD rovibrational distributions

Sample data for the LIF excitation spectra of OH and OD following 193 nm photolysis of jet-cooled H<sub>2</sub>O and D<sub>2</sub>O are shown in Fig. 4. Results are shown in Figs. 7(a) and 7(b) for percent population in three of the four fine structure manifolds. To ensure reliable statistics, the distributions are averaged over three sets of measurements, each set consisting of three spectral scans of OH and OD from the photodissociation of isotopically pure samples. The excellent quality of data reproducibility is reflected in the (1σ) error bars for the full dataset. Also shown for comparison in Fig. 7(c) are OH distributions reported for 157 nm photolysis of jet-cooled H<sub>2</sub>O in the Franck–Condon regime.<sup>4</sup>

The trends in the OH and OD populations at 193 nm are similar; the Π<sup>+</sup> distributions display a monotonic decrease with increasing  $N$  while populations in the Π<sup>-</sup> manifold peak at  $N=2$ . Both distributions are rotationally cold; the mean rotational energies (averaged over the three fine structure levels) are found to be ~200 cm<sup>-1</sup> for both OH and OD. This is also comparable to the degree of rotational excitation observed from vibrationally mediated IR+248 nm OH bond cleavage studies in  $v_{\text{OH}}=3$  excited HOH and HOD species in our laboratory,<sup>16,17</sup> which sample a similar total energy (~50 900 cm<sup>-1</sup> vs 51 813 cm<sup>-1</sup>) on the electronically excited potential surface. Finally, the spectral region near the  $\tilde{A}^2\Sigma(v'=1) \leftarrow \tilde{X}^2\Pi(v''=1)$  transitions in OH and OD are checked for vibrationally excited products. No intensity in any  $v''>0$  bands is observed, which establishes upper limits for  $v''=1/v''=0$  of <0.2% and <10% in the OH and OD products, respectively. Note that although there are similar qualitative trends between the 193 and 157 nm data, clear differences exist between the relative magnitudes of Π<sup>+</sup>, Π<sup>-</sup> components, which are discussed later in Sec. V C.

### B. UV absorption cross section ratio for H<sub>2</sub>O and D<sub>2</sub>O at 193 nm

Since all of the photofragment populations are in  $v=0$ , the relative absorption cross section ratio,  $\sigma_{\text{H}_2\text{O}}/\sigma_{\text{D}_2\text{O}}$ , at 193

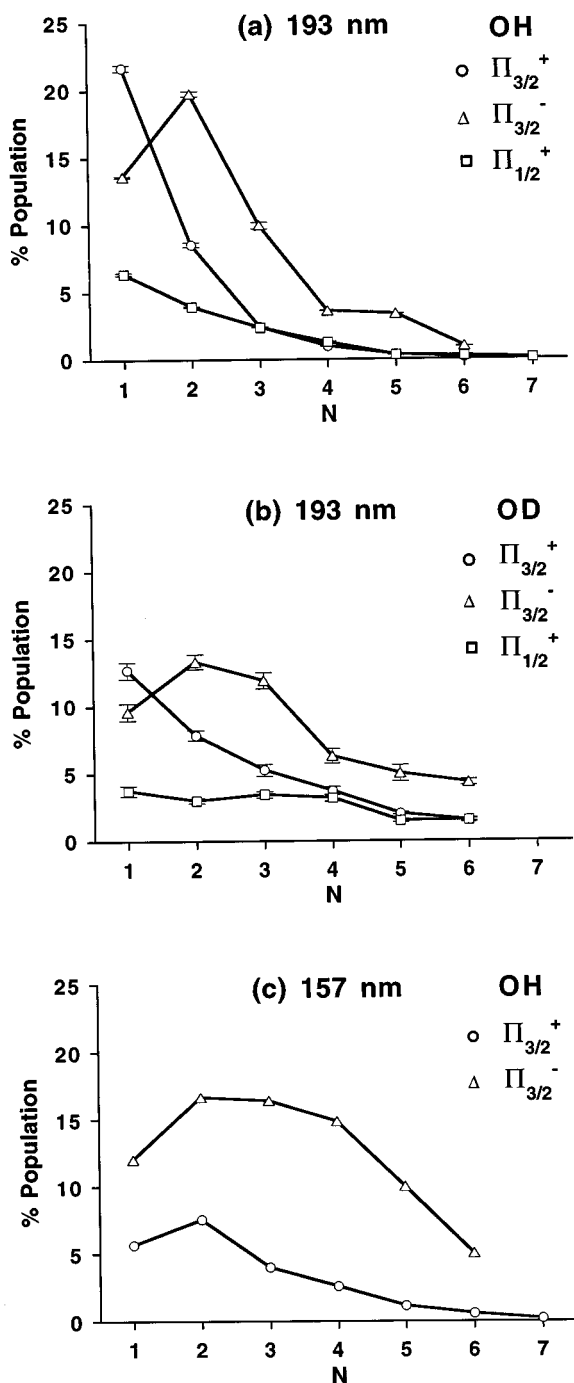


FIG. 7. Percent rotational state populations (with  $1\sigma$  error bars) in the  $\Pi_{3/2}^+$  (circles),  $\Pi_{1/2}^+$  (squares), and  $\Pi_{3/2}^-$  (triangles) levels of OH (a) and OD (b) from the 193 nm photolysis of jet-cooled samples of H<sub>2</sub>O and D<sub>2</sub>O. For comparison, OH populations obtained from 157 nm photolysis of jet-cooled H<sub>2</sub>O (Ref. 4) are shown in (c). The distributions reflect photolysis from  $0_{00}$  and  $1_{01}$  rotational states of H<sub>2</sub>O and D<sub>2</sub>O with population ratios of 3:1 and 1:2, respectively.

nm can be obtained from the OH/OD rotational state populations summed over each of the fine structure (i.e.,  $\Lambda$ -doublet and spin orbit) levels. These numbers are given separately in Table II for the three levels of OH and OD observed ( $\Pi_{3/2}^+$ ,  $\Pi_{1/2}^+$ , and  $\Pi_{3/2}^-$ ); averaged over these three

TABLE II. Relative and percent populations in the fine structure and  $\Lambda$ -doublet manifolds of OH and OD from the photolysis of H<sub>2</sub>O and D<sub>2</sub>O at 193 nm.

Manifold	Relative population		Percent population	
	(OD)	(OH)	(OD)	(OH)
$\Pi_{3/2}^+$	0.331(9) <sup>a</sup>	19.2(2)	33.1%	34.2%
$\Pi_{1/2}^+$	0.164(6)	8.2(1)	16.4%	14.6%
$\Pi_{3/2}^-$	0.505(13)	28.7(2)	50.5%	51.2%

<sup>a</sup>Error bars are  $1\sigma$  in the least significant digit.

fine structure levels,  $\sigma_{\text{H}_2\text{O}}/\sigma_{\text{D}_2\text{O}}$  is  $56 \pm 10$ . Any error due to lack of data on the  $\Pi_{1/2}^-$  level can be estimated by comparing the OH/OD fractional populations for the three fine structure levels observed (see Table II), which differ at most by a few percent. A small but quantifiable correction arises from the residual HOD impurity in the D<sub>2</sub>O. From detailed studies<sup>25</sup> of 193 nm photolysis of isotopic H<sub>2</sub>O/D<sub>2</sub>O/HOD mixtures, the branching fraction,  $\sigma_{\text{OD}}^{\text{HOD}}/\sigma_{\text{OD}}^{\text{D}_2\text{O}}$ , has been shown to be 24.6(6.5):1. Thus, the experimental 0.5% HOD impurity in the original sample leads to only a small additional OD signal, which can be explicitly accounted for to yield  $\sigma_{\text{H}_2\text{O}}/\sigma_{\text{D}_2\text{O}} = 64(10):1$  (see Table III). This is substantially smaller than the theoretical predictions by Schinke and co-workers<sup>20</sup> of  $>200:1$  and well outside any uncertainties due to isotopic sample purity.

### C. $\Lambda$ -doublet populations ratios

An additional window into the dissociation dynamics is provided by populations in the two  $\Lambda$ -doublet levels, which can be determined from the  $\Pi_{3/2}^-/\Pi_{3/2}^+$  ratios. These ratios for OH and OD are shown in Figs. 8(a) and 8(b) as a function of  $N$ . The data clearly indicate a preference to photolyze into the  $\Pi^-$  vs  $\Pi^+$  manifold, which reflects a strong population inversion, particularly evident for OH at higher values of  $N$ . While the OD data exhibit a similar trend and degree of  $N$ -dependent structure, the overall magnitude of the population inversion for OD at high  $N$  is smaller by roughly a factor of 2. Though there also appears to be faster  $N$ -dependent structures in these ratios for both OH and OD photofragments, this overall increase in the observed ratios with  $N$  is largely a result of the  $\Lambda$ -doublet mixing that occurs in the OH/OD product and first observed for 157 nm photolysis of jet-cooled H<sub>2</sub>O in the Franck–Condon absorption region [see Fig. 8(c)]. As noted by Andresen *et al.* in the 157 nm study,<sup>4</sup> the high- $J$  limiting case descriptions of  $\Pi^-$  and

TABLE III. Predicted and measured relative absorption cross section ratios determined from photolysis of H<sub>2</sub>O and D<sub>2</sub>O at 193 and 157 nm.

	193 nm	Predicted <sup>a</sup>	157 nm <sup>b</sup>	Predicted <sup>c</sup>
$\sigma_{\text{H}_2\text{O}}/\sigma_{\text{D}_2\text{O}}$	$64 \pm 10$	$>200$	$1.16 \pm 0.04$	$1.12 \pm 0.05$

<sup>a</sup>Reference 20.

<sup>b</sup>Reference 34.

<sup>c</sup>Reference 3.

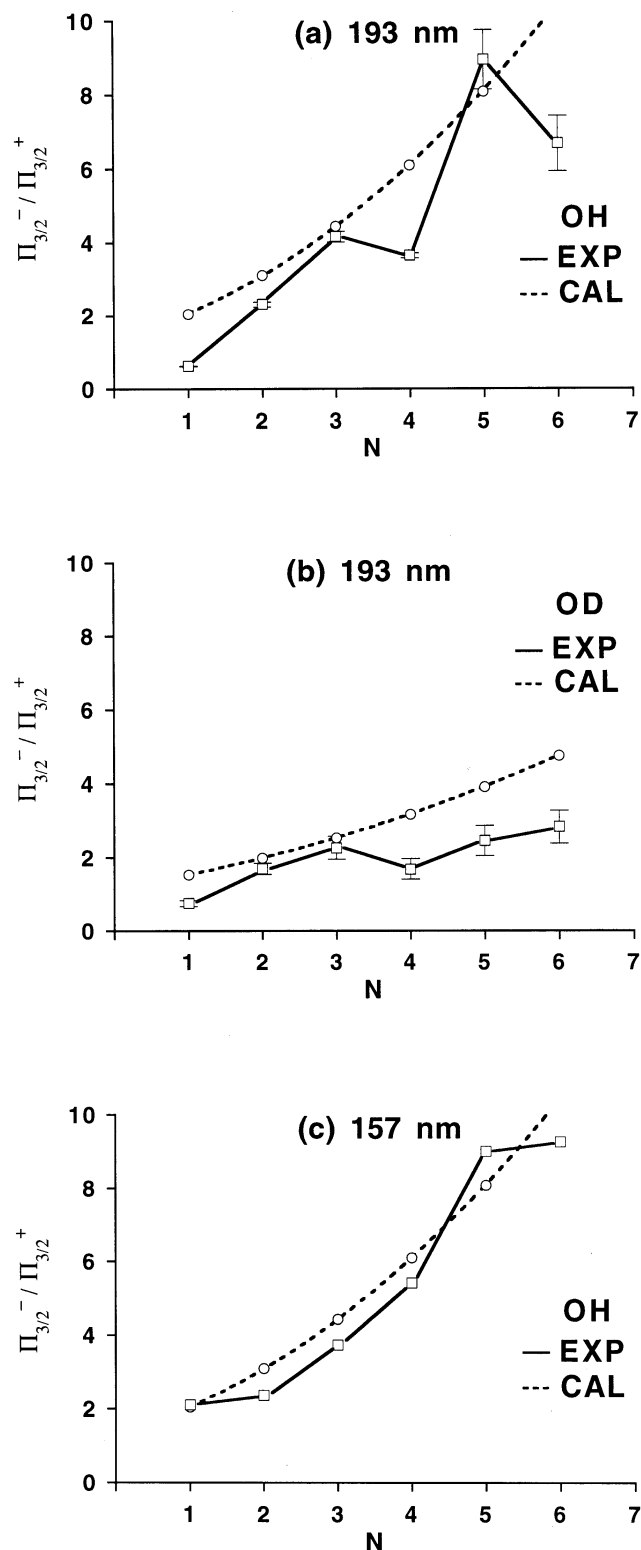


FIG. 8.  $\Lambda$ -doublet ratios in the  $\Pi_{3/2}^+$  and  $\Pi_{3/2}^-$  levels as a function of rotational quantum number  $N$  for 193 nm photolysis of H<sub>2</sub>O (a) and D<sub>2</sub>O (b). The ratios for jet-cooled H<sub>2</sub>O at 157 nm are shown in (c) (Ref. 4). Also included are model predictions (dashed lines) for planar dissociation of H<sub>2</sub>O and D<sub>2</sub>O that account for  $\Lambda$ -doublet mixing in the products (Ref. 4) [see Eqs. (3)–(4)]. The  $p\pi$  orbital alignment in OH is predicted to increase with  $N$  at twice the rate of increase in OD, due to faster rotational decoupling of spin from the nuclear axis of OH.

$\Pi^+$   $\Lambda$ -doublet states of OH correspond to the unpaired  $p\pi$  lobe perpendicular to ( $\phi_{\perp}$ ), or in the plane of ( $\phi_{\parallel}$ ) the OH rotation, respectively. For arbitrary  $J$ , however, these two OH wave functions can be expanded in terms of these two basis states as  $\Psi = c_J\phi_{\perp} + d_J\phi_{\parallel}$ , where the  $J$  dependence of the mixing coefficients is related to the degree of  $p\pi$  lobe alignment by<sup>4,32</sup>

$$c_J^2 = \frac{1}{2} + \left( 4 + \frac{(\lambda - 2)^2}{(J - 1/2)(J + 3/2)} \right)^{-1/2} \quad (3)$$

In Eq. (3),  $\lambda = A/B$  is the ratio of the  $A$  spin-orbit splitting coefficient and  $B$  rotational constant. In the absence of parent rotation, it can be further argued that electronic excitation of the  $1b_1$  orbital perpendicular to the H<sub>2</sub>O plane correlates exclusively to the component of the  $p\pi$  lobe of OH perpendicular to its rotation plane, as required by symmetry conservation during the dissociation. Hence, the  $\Lambda$ -doublet population ratio can be derived in terms of the mixing coefficients that describe the OH wave function,<sup>4,32</sup>

$$\frac{\Pi^-}{\Pi^+} = \frac{c_J^2}{d_J^2} = \frac{c_J^2}{1 - c_J^2} \quad (4)$$

From the nearly quantitative agreement of this model with the jet-cooled data of Andresen and co-workers at 157 nm, the authors suggested that the underlying dissociative mechanism of H<sub>2</sub>O reflects prompt formation of OH from a planar intermediate having its singly occupied  $p\pi$  lobe perpendicular to the parent symmetry plane.

The predicted  $\Lambda$ -doublet ratios from Eqs. (3) and (4) for both OH and OD are shown with dashed lines in Fig. 8 using the known values of  $\lambda_{\text{OH}} = -7.502$  and  $\lambda_{\text{OD}} = -14.072$ . The model does correctly predict the *relative* magnitudes of the  $\Lambda$ -doublet ratios; the ratios observed for OD are roughly one-half those for OH. The origin of the differences arises primarily from the different rotational constants<sup>33</sup> of the products ( $B_0^{\text{OH}} = 18.535 \text{ cm}^{-1}$ ;  $B_0^{\text{OD}} = 9.8788 \text{ cm}^{-1}$ ) and enter into the model through  $\lambda = A/B$  in Eq. (3). However, unlike the jet-cooled data at 157 nm, the 193 nm ratios for both OH and OD exhibit much more  $N$ -dependent structure and are consistently *lower* (by as much as two-fold) than predicted from this simple planar recoil model. It is worth noting that deviations from the predicted  $\Lambda$ -doublet inversion have been observed for 157 nm photolysis of H<sub>2</sub>O at *room temperature*; specifically, “statistically” distributed populations with  $\Pi^-/\Pi^+$  ratios near unity are found for all  $N$  states of OH and OD. This “smearing out” of the  $\Lambda$ -doublet population inversion for room temperature samples has been explained as a result of additional  $1b_1$  orbital mixing on the parent with the product states caused by out-of-plane rotational motion of the parent and its plane of symmetry during the dissociation. In the present jet-cooled studies of H<sub>2</sub>O and D<sub>2</sub>O at 193 nm; however, the initial rotational state populations are cooled into the lowest rotational states permitted by nuclear spin symmetry, i.e.,  $0_{00}$  and  $1_{01}$ , in 1:3 and 2:1 ratios, respectively. Furthermore, the only excited state,  $1_{01}$ , corresponds primarily to in-plane rotation of the molecule, which presumably would be less effective at diminishing the

$\Lambda$ -doublet population inversion. Finally, these are the *same* initial levels sampled in the jet-cooled studies in the Franck–Condon regime at 157 nm, which, as shown in Fig. 8(c), yield  $\Lambda$ -doublet inversions in nearly quantitative agreement with theoretical predictions for a prompt, planar dissociation event.

#### D. Spin–orbit state populations

The population ratios in the  $\Pi_{3/2}^+$  and  $\Pi_{1/2}^+$  fine structure levels are determined for each rotational state pair in order to identify preferential spin–orbit state selectivity in the far off-resonance 193 nm photodissociation dynamics of H<sub>2</sub>O and D<sub>2</sub>O. The  $\Pi_{3/2}^+/\Pi_{1/2}^+$  population ratios are corrected for lower state degeneracy by  $N/(N+1)$  and shown in Figs. 9(a) and 9(b), where unity represents a statistical distribution of the two fine structure levels. The results indicate a similar, highly structured dependence on  $N$  for both OH and OD, with values deviating at low  $N$  by almost a factor of 2 from the statistical limit.

The fact that there are any distinct spin-state preferences is interesting in itself, since this is the largest selectivity reported in any previous photolysis studies of H<sub>2</sub>O and D<sub>2</sub>O in the Franck–Condon allowed region. Specifically, as shown in Fig. 9(c) for the photolysis of water at 157 nm, there is only a modest (<10%) preference indicated for the  $\Pi_{1/2}^+$  level at low  $N$  values, with essentially no spin orbit preference noted for the corresponding OD fragment. It is worth noting that the 157 nm data are only reported for room temperature H<sub>2</sub>O samples, which, in principle, might be influenced by initial thermal rotational motion. However, similarly near-statistical spin orbit distributions have also been reported for vibrationally mediated photolysis of pure quantum states in the Franck–Condon regime, for example, as observed from 193 nm photolysis of the  $0_{00}|01\rangle^-$  level of H<sub>2</sub>O.<sup>5</sup> The clearly *nonstatistical* spin state ratios observed in the present study, as well as the strong similarity between OH and OD distributions, suggest important dynamical differences between resonant and far off-resonant photodissociation of water.

## VI. DISCUSSION

As noted in the Introduction, there has been a remarkable series of theoretical successes in predicting quantum state resolved product state distributions from initially prepared states of H<sub>2</sub>O and isotopomers. Of particular relevance to this work are the observed and predicted absorption cross section ratios for on-resonance photolysis of H<sub>2</sub>O and D<sub>2</sub>O at 157 nm,<sup>4,34</sup> which samples Franck–Condon allowed regions of the upper and lower potential surfaces. The results are summarized in Table III. The theoretical calculations by Imre and Zhang<sup>3</sup> on the Reimers–Watts<sup>35</sup> (RW) and Staemmler–Palma<sup>19</sup> (SP) potential surfaces predicted an isotope effect,  $\sigma_{\text{H}_2\text{O}}/\sigma_{\text{D}_2\text{O}} = 1.12 \pm 0.05$ , in quantitative agreement with the experimental value<sup>34</sup> of  $1.16 \pm 0.04$ . By way of contrast, the present study at 193 nm yields an isotope effect of  $64 \pm 10$ , which is more than three-fold smaller than the

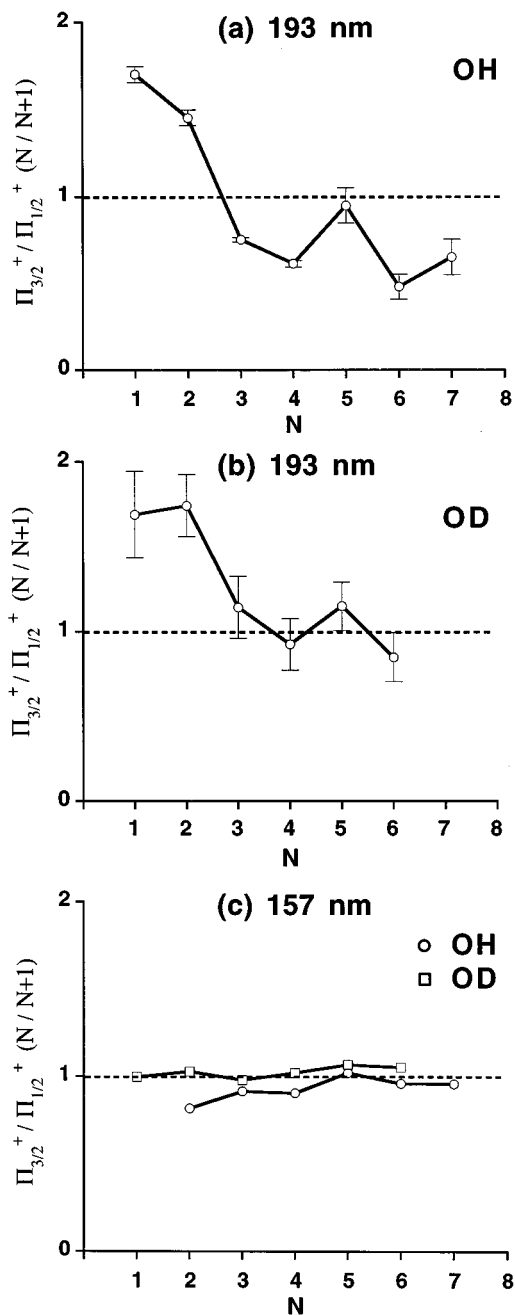


FIG. 9. Population ratios of OH (a) and OD (b) between the  $\Pi_{3/2}^+$  and  $\Pi_{1/2}^+$  manifolds as a function of rotational quantum number  $N$ . The spin-state ratios are first corrected for the  $2J+1$  state degeneracies with the factor  $N/N+1$  ( $J=N+1/2$  for  $\Omega=3/2$  and  $J=N-1/2$  for  $\Omega=1/2$ ); a ratio of 1:1 therefore corresponds to a statistical distribution over the two spin levels. Compared to the unity ratios obtained at 157 nm for room temperature H<sub>2</sub>O and D<sub>2</sub>O (c), significantly *nonstatistical* spin-state distributions are apparent for 193 nm photolysis.

predicted ratio<sup>20</sup> of  $>200$  calculated on the Sorbie and Murrell (SM) and SP potential surfaces. Even more dramatic discrepancies are found for photolysis of HOD at 193 nm between observed<sup>25</sup> [12(5):1] and predicted ( $>100$ :1) OH/OD branching ratios.<sup>20</sup> Given the simplicity of the

H<sub>2</sub>O/HOD/D<sub>2</sub>O molecular system and the quantitative success of previous calculations in the Franck–Condon allowed regime, these anomalous isotope effects are significant and warrant further consideration.

It is first important to demonstrate that these discrepancies are ‘robust,’ i.e., substantially outside the range due simply to uncertainties on the upper and lower potential surfaces. The total absorption cross section,  $\sigma(E)$ , is given by Fermi’s Golden Rule,<sup>2</sup>

$$\sigma(E) = \sum_n \frac{4\pi}{3hc} E |\langle \Psi_2^{(n)} | \mu_e | \Psi_1 \rangle|^2, \quad (5)$$

where the sum is over all vibrational product channels. No vibrationally excited OH/OD products are observed<sup>25</sup> at 193 nm and, therefore, the sum in Eq. (5) reduces to the single lowest term. The  $\mu_e$  changes very slowly with internuclear distance and in the Born–Oppenheimer approximation is identical for H<sub>2</sub>O and D<sub>2</sub>O. In the context of a Franck–Condon model, therefore, the total cross sections and cross section ratios are dominated by the overlap between the lower state bound and excited state continuum wave functions. Since our present goal is simply to assess the sensitivities of these cross section ratios to uncertainties in the upper/lower potential surfaces, we utilize 1D analysis in the coordinate of the H–OH or D–OD bond that is photolyzed while the remaining stretch/bend coordinates are held fixed at 0.9710 Å and 104.52°, respectively. This approximation is particularly reasonable for far off-resonance photolysis at 193 nm since the wave function overlap region occurs for one highly stretched bond, with the other bond length essentially at the equilibrium geometry of the asymptotic photofragment.

This 1-D approach allows one to take advantage of elegant semiclassical treatments by Miller and Child<sup>36</sup> for calculating overlap matrix elements. For the current case of non-Franck–Condon excitation, the lower state potential  $V_1(R)$  has an *outer* classical turning point ( $a_1$ ) that is less than the *inner* classical turning point ( $a_2$ ) for the continuum wave function on the upper surface  $V_2(R)$ , and thus the matrix elements are dominated by integration over the classically forbidden regions for both upper and lower states ( $a_1 < R < a_2$ ). If one represents the two wave functions in this region by WKB wave functions, the matrix elements in Eq. (5) can be expressed as a function of  $a_1, a_2$  and the Condon point ( $R_x$ ), i.e., the photolysis fragment bond separation for which  $V_2(R_x) = V_1(R_x) + \hbar\omega$ . With uniform Airy approximation methods,<sup>36</sup> the desired Franck–Condon overlap matrix elements in Eq. (5) are found to be

$$\begin{aligned} \langle \Psi_2 | \mu_e(R) | \Psi_1 \rangle &= \left( \frac{2\bar{\omega}}{v(R_x) |\Delta F(R_x)|} \right)^{1/2} \mu_{12}(R_x) \\ &\times \eta^{1/4}(R_x) \text{Ai}[\eta(R_x)], \end{aligned} \quad (6)$$

where  $\bar{\omega}$  is the semiclassical period of vibrational motion in the lower electronic state and Ai is the Airy function. In Eq. (6),  $\Delta F(R_x)$  is the force difference,

$$\Delta F(R_x) = \left( \frac{dV_1(R)}{dR} - \frac{dV_2(R)}{dR} \right)_{R_x}, \quad (7)$$

and  $v(R_x)$  is the classical speed,

$$v(R_x) = \left( \frac{2[V_1(R_x) - E_1]}{m} \right)^{1/2}, \quad (8)$$

where  $m$  is the reduced mass of the photolysis fragments. Each of these expressions is evaluated at  $R_x$ , where the WKB phase integral,

$$\eta(R_x) = \left( \frac{3}{2} \int_{a_1}^{R_x} \frac{|p_1(R)| dR}{\hbar} + \frac{3}{2} \int_{R_x}^{a_2} \frac{|p_2(R)| dR}{\hbar} \right)^{2/3}, \quad (9)$$

reaches an extremum as a function of the classical momenta,

$$p_i(R) = \sqrt{2m[E_i - V_i(R)]}, \quad (10)$$

on the upper and lower potential. The quantitative accuracy of these semiclassical expressions for 1D matrix elements in the classically forbidden region is excellent, as tested by comparison between the predictions of Eq. (6) and exact numerical integration over bound and continuum wave functions. By way of example, for the Sorbie–Murrell ground state and Staemmler–Palma surfaces, Eq. (6) predicts an isotope ratio of  $\sigma_{\text{H}_2\text{O}}/\sigma_{\text{D}_2\text{O}} = 203$ , which is in essentially quantitative agreement with the  $\geq 200$  value obtained by Schinke and co-workers<sup>20</sup> on these surfaces from more rigorous full quantum scattering calculations.

To assess how uncertainties in the upper/lower state potentials translate into uncertainties in these isotope ratios, we are primarily concerned with surface accuracy corresponding to OH and OD bond lengths in the 1.3–1.4 Å region (see Fig. 10). The ground electronic surface for such extended OH/OD bond lengths has been well sampled via high overtone spectroscopic studies up to 17 500 cm<sup>-1</sup>.<sup>37</sup> Two widely used semiempirical potentials constructed from this data are the Sorbie and Murrell<sup>11,18</sup> (SM) and the Reimer and Watts<sup>35</sup> (RW) surfaces. Eigenvalues have been calculated on the SM PES up through 7500 cm<sup>-1</sup>; agreement with experimental term values and band origins is better than 1%.<sup>9,18</sup> For the RW potential, comparisons of eigenvalues<sup>37</sup> have been made for energies up through 17 500 cm<sup>-1</sup> with errors of less than 0.3%.<sup>35</sup> A much more extensively tested potential surface for H<sub>2</sub>O has been proposed by Tennyson and co-workers,<sup>38</sup> who claim <0.01% agreement with high overtone rovibrational spectroscopic studies up to energies of >20 000 cm<sup>-1</sup>.

Independent experimental tests of the accuracy of the ground state potentials have come from comparisons of the predicted and experimental resonance Raman spectrum measured by Sension *et al.*<sup>39</sup> For Raman pump wavelengths that access the <sup>1</sup>B<sub>1</sub> state in the wavelength range of 160–171 nm,<sup>39</sup> the observed spectrum corresponds to stimulated resonance Raman excitation of highly excited totally symmetric vibrational modes of up to five quanta on the ground state PES. Imre and co-workers,<sup>3,40</sup> using time-dependent methods and the FC model, find that only slight changes in the RW surface result in large changes in calculated Raman intensi-

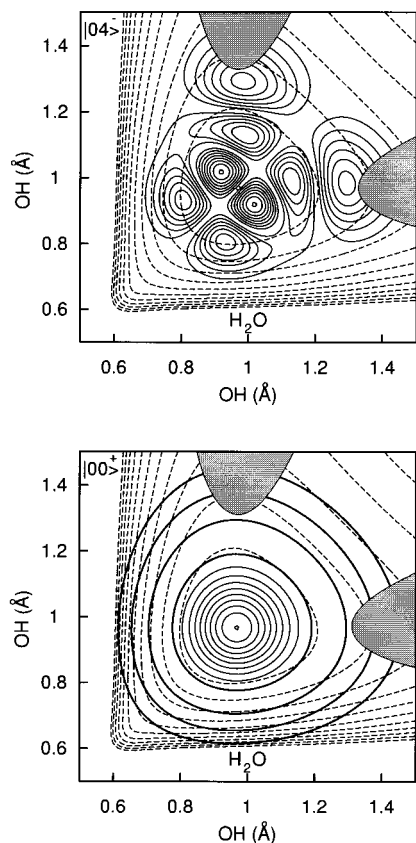


FIG. 10. The  $|04\rangle^-$  (top panel) and  $|00\rangle^+$  (bottom panel) vibrational wave functions of H<sub>2</sub>O calculated on the SM ground state PES. Cuts through the SP PES are shown with shaded regions for photolysis wavelengths greater than 193 nm (top panel) and greater than 266 nm (bottom panel) relative to the  $|00\rangle^+$  and  $|04\rangle^-$  vibrational energies. These plots illustrate that the regions accessed by far off-resonance photolysis at 193 nm are similar to those sampled on resonance by IR overtone excitation at 723 nm followed by photolysis at 266 nm.<sup>7</sup>

ties and conclude that this is an accurate potential for H<sub>2</sub>O. Schinke and co-workers<sup>41</sup> have performed similar studies using the SM PES at fixed bond angles of 104° and find good but somewhat less satisfying agreement with the observed ground state energy levels and Raman intensities. Observed minus calculated energies are typically better than 300 cm<sup>-1</sup> for levels up through the third overtone ( $\approx 14\,000$  cm<sup>-1</sup>); this suggests a reasonable upper limit of  $\pm 1$  kcal/mole uncertainty in the SM ground state potential surface in this OH/OD bond length region. This is large by current standards for such a small molecule, which is why predictions on the much better determined H<sub>2</sub>O 3D potential surface of Tennyson and co-workers are also included.<sup>38</sup>

With regard to the excited singlet state of H<sub>2</sub>O, all photodissociation calculations are based on the *ab initio* surface of Staemmler and Palma.<sup>19</sup> Accuracy estimates based on spectroscopic data of H<sub>2</sub>O and D<sub>2</sub>O are difficult due to the diffuse nature of the spectra<sup>12,42</sup> although the absorption maximum at 167 nm is reproduced, and good agreement is found with the RKR curves<sup>43</sup> of OH(<sup>2</sup>Π) in the region of the minimum in the exit channel. Moreover, several indirect tests of SP surface accuracy have come from a detailed com-

TABLE IV. 1D semiclassical modeling of Franck–Condon factors and isotope effects for photolysis of H<sub>2</sub>O/D<sub>2</sub>O at 193 nm. The results are obtained from Eq. (6) for each ground state potential surface with the unphotolyzed OH/OD bond fixed at 0.9710 Å and the HOH/DOD bond angle fixed at 104.52° (see the text for details). The electronically excited surface is vertically offset by the amount shown to test for sensitivity in the calculation to  $\pm 1$  kcal/mole.

Lower PES	Upper PES	$\sigma_{\text{H}_2\text{O}}/\sigma_{\text{D}_2\text{O}}$
SM <sup>a</sup>	SP <sup>b</sup> - 1.0 kcal/mole	150
SM <sup>a</sup>	SP <sup>b</sup>	203
SM <sup>a</sup>	SP <sup>b</sup> + 1.0 kcal/mole	244
RW <sup>c</sup>	SP <sup>b</sup>	712
Tennyson <sup>d</sup>	SP <sup>b</sup>	748
Experiment (this work)		64(10)

<sup>a</sup>Reference 18.

<sup>b</sup>Reference 19.

<sup>c</sup>Reference 35.

<sup>d</sup>Reference 38.

parison of theoretical predictions of Schinke *et al.* with the results of vibrationally mediated photolysis experiments by Crim and co-workers.<sup>6</sup> Most relevant to our results is the study of UV photolysis of  $|04\rangle^-$  by Vander Wal *et al.*,<sup>7</sup> where experimental cross sections have been measured relative to the value determined at 266 nm and compared directly with the predictions from wave packet propagation calculations of Weide *et al.*<sup>14</sup> on the SM and SP PES. The agreement is qualitatively excellent, reproducing the oscillatory nature of the relative cross sections over the experimental range of photolysis wavelengths. However, a small phase shift in this oscillation between experiment and theory was observed that could be eliminated by lowering the excited state PES by 50 meV ( $\approx 1.15$  kcal/mole); this provides a rough estimate of  $\pm 1$  kcal/mole uncertainty for the upper/lower potential surfaces near this OH bond length. Again, it is worth noting that these uncertainties are considerably higher than current *ab initio* standards for systems with such few electrons. In any event,  $\pm 1$  kcal/mole uncertainty constitutes a fairly conservative estimate for comparison with experiment.

The effect of propagating uncertainties on the predicted isotope ratios at 193 nm is obtained from Eq. (6) by shifting the ground and excited potential surfaces and recalculating the ratio of H<sub>2</sub>O/D<sub>2</sub>O absorption cross sections. As summarized in Table IV, these results clearly indicate a sensitivity in the isotope ratios at the level of  $\pm 25\%$  for a shift in potential surfaces by  $\pm 1$  kcal/mole, which is more than an order of magnitude too small to account for the 300% discrepancies observed between theory and experiment. Table IV also contains the semiclassical predictions of H<sub>2</sub>O/D<sub>2</sub>O isotope ratios for 193 nm excitation on the potential surfaces of Riemer–Watts<sup>35</sup> and Tennyson.<sup>38</sup> For both of these other surfaces, the discrepancy between experiment and theory is increased even further, with predicted ratios now as much as 100-fold larger than experimentally observed. Though the most detailed theoretical studies of UV photolysis dynamics have been based on the Sorbie Murrell ground state surface, this comparison makes clear that predictions for empirically well-determined ground state surfaces are even more in dis-

agreement with the current experiment results.

For such a well-studied benchmark photolysis system, the magnitude of this discrepancy between theory and experiment is significant. Though the reason for this discrepancy is not yet clear, the following comments are offered as possible directions for investigation. The first is that the Franck–Condon model assumes Born–Oppenheimer decoupling of nuclear and electronic degrees of freedom in the photoexcitation step. However, the overlap matrix elements for Franck–Condon vertical transitions are exponentially suppressed due to the far off-resonance nature of the UV excitation, which in turn translates into an exponentially large advantage for nonvertical transition processes. It is therefore conceivable that the extreme non-Franck–Condon nature of the excitation provides sufficient contrast for non-Born–Oppenheimer effects to influence the photolysis dynamics for such light atom systems. A second possibility is that at these longer excitation wavelengths, nonadiabatic final state interactions between the various exit channels cannot be neglected. One extreme example of this would be if direct excitation to the lowest *triplet* state were weakly contributing to the absorption, which would be red-shifted from the lowest singlet band and therefore more resonant with 193 nm excitation. This intriguing possibility is addressed elsewhere by Schinke and co-workers,<sup>20</sup> based on an *ab initio* calculation of the triplet surface and comparison of the experimentally measured OH/OD bond photolysis propensities in HOH, DOD, and HOD isotopomers.

## VII. SUMMARY AND CONCLUSIONS

By virtue of the cooling in the supersonic jet, H<sub>2</sub>O and D<sub>2</sub>O are vibrationally and rotationally state selected in their zero-point vibrational levels and 0<sub>00</sub> and 1<sub>01</sub> rotational states prior to being photolyzed at 193 nm. Both OH or OD products are found to be vibrationally cold. The OH/OD rotational distributions from non-Franck–Condon photolysis at 193 nm are qualitatively similar to those found from photolysis in the Franck–Condon region at 157 nm, though more *N*-dependent structure is exhibited. The  $\Lambda$ -doublet and spin orbit distributions are clearly not in good agreement with the Franck–Condon model predictions. Specifically, the  $\Lambda$ -doublet populations are much less inverted for both OH and OD distributions, which is contrary to the behavior observed at 157 nm for a model of prompt, in-plane dissociation of the H<sub>2</sub>O molecule and the absence of exit channel interactions. Furthermore, the spin orbit distributions with 193 nm photolysis are significantly nonstatistical and dependent on rotational state. This is in clear contrast to the nearly statistical spin orbit distributions observed for all other photolysis studies in the Franck–Condon regime, and indicate that photolysis dynamics in this regime is not currently well predicted from Franck–Condon model calculations.

As one direct point of quantitative comparison with theory, the experimental isotope ratio for 193 nm photolysis of H<sub>2</sub>O vs D<sub>2</sub>O has been measured to be  $\sigma_{\text{H}_2\text{O}}/\sigma_{\text{D}_2\text{O}} = 64 \pm 10$ ; this is more than three-fold smaller than current Franck–Condon model calculations by Schinke and co-

workers using the ground state PES of Sorbie and Murrell and the excited state PES of Staemmler and Palma. Within the context of such a theoretical Franck–Condon model, this discrepancy is robust; from a 1D semiclassical analysis, shifts in the potential surface by  $\pm 1$  kcal/mole only translate into  $\lesssim 25\%$  changes in the predicted isotope ratio. Even more dramatic discrepancies in these isotope ratios (as large as 100-fold) are predicted from other empirically determined potentials for the ground state surface. This body of results indicates that the photolysis dynamics of even simple “benchmark” molecules such as H<sub>2</sub>O and D<sub>2</sub>O in the extreme non-Franck–Condon regime warrants further theoretical attention.

## ACKNOWLEDGMENTS

This work has been supported by grants from the National Science Foundation. Numerous stimulating discussions with Dr. Reinhard Schinke and Professor Jonathon Tennyson are gratefully acknowledged.

- <sup>1</sup>H. Guo and J. N. Murrell, *Mol. Phys.* **65**, 821 (1988); S. Hennig, V. Engel, and R. Schinke, *Chem. Phys. Lett.* **149**, 455 (1988); K. Kühl and R. Schinke, *ibid.* **158**, 81 (1989); R. Schinke, V. Engel, and V. Staemmler, *J. Chem. Phys.* **83**, 4522 (1985).
- <sup>2</sup>P. Andresen and R. Schinke, in *Molecular Photodissociation Dynamics*, edited by M. N. R. Ashfold and J. E. Baggott (Royal Society of Chemistry, London, 1987); R. Schinke, in *Photodissociation Dynamics* (Cambridge University Press, Cambridge, 1993).
- <sup>3</sup>D. J. Imre and J. Zhang, *Chem. Phys.* **139**, 89 (1989).
- <sup>4</sup>P. Andresen, G. S. Ondrey, B. Titze, and E. W. Rothe, *J. Chem. Phys.* **80**, 2548 (1984).
- <sup>5</sup>P. Andresen, V. Beushausen, D. Häusler, H. W. Lülfe, and E. W. Rothe, *J. Chem. Phys.* **83**, 1429 (1985); D. Häusler, P. Andresen, and R. Schinke, *ibid.* **87**, 3949 (1987).
- <sup>6</sup>R. L. Vander Wal and F. F. Crim, *J. Chem. Phys.* **93**, 5331 (1989); R. L. Vander Wal, J. L. Scott, and F. F. Crim, *J. Chem. Phys.* **92**, 803 (1990); R. L. Vander Wal, R. J. Scott, F. F. Crim, K. Weide, and R. Schinke, *ibid.* **94**, 3548 (1991); R. Schinke, R. L. Vander Wal, J. L. Scott, and F. F. Crim, *ibid.* **94**, 283 (1991).
- <sup>7</sup>R. L. Vander Wal, J. L. Scott, and F. F. Crim, *J. Chem. Phys.* **94**, 1859 (1991).
- <sup>8</sup>M. Brouard, S. R. Langford, and D. E. Manolopoulos, *J. Chem. Phys.* **101**, 7458 (1994).
- <sup>9</sup>R. T. Lawton and M. S. Child, *Mol. Phys.* **40**, 773 (1980); **37**, 1799 (1979).
- <sup>10</sup>V. Engel, R. Schinke, and V. Staemmler, *Chem. Phys. Lett.* **130**, 413 (1986).
- <sup>11</sup>V. Engel, R. Schinke, and V. Staemmler, *J. Chem. Phys.* **88**, 129 (1988).
- <sup>12</sup>H.-t. Wang, W. S. Felps, and S. P. McGlynn, *J. Chem. Phys.* **67**, 2614 (1977).
- <sup>13</sup>A. U. Grunewald, K.-H. Gericke, and F. J. Comes, *Chem. Phys. Lett.* **133**, 501 (1987).
- <sup>14</sup>K. Weide, S. Hennig, and R. Schinke, *J. Chem. Phys.* **91**, 7630 (1989).
- <sup>15</sup>D. F. Plusquellic, O. Votava, and D. J. Nesbitt, *J. Chem. Phys.* **101**, 6365 (1994).
- <sup>16</sup>O. Votava, D. F. Plusquellic, J. R. Fair, E. Riedle, and D. J. Nesbitt, *J. Chem. Phys.* (in press).
- <sup>17</sup>O. Votava, D. F. Plusquellic, and D. J. Nesbitt (in preparation).
- <sup>18</sup>K. S. Sorbie and J. N. Murrell, *Mol. Phys.* **29**, 1387 (1975); *ibid.*, **31**, 905 (1956).
- <sup>19</sup>V. Staemmler and A. Palma, *Chem. Phys.* **93**, 63 (1985).
- <sup>20</sup>T. Schröder and R. Schinke (manuscript in preparation).
- <sup>21</sup>C. M. Lovejoy and D. J. Nesbitt, *Rev. Sci. Instrum.* **58**, 807 (1987); C. M. Lovejoy and D. J. Nesbitt, *J. Chem. Phys.* **86**, 3151 (1987).

- <sup>22</sup>J. A. Coxon, *Can. J. Phys.* **58**, 933 (1980); M. A. A. Clyne, J. A. Coxon, and A. R. Woon Fat, *J. Mol. Struct.* **46**, 146 (1973).
- <sup>23</sup>W. A. Majewski and W. L. Meerts, *J. Mol. Spectrosc.* **104**, 271 (1984); W. A. Majewski, D. F. Plusquellic, and D. W. Pratt, *J. Chem. Phys.* **90**, 1362 (1989).
- <sup>24</sup>J. D. Kilkenny and M. S. White, *Phys. Lett.* **55A**, 209 (1975); R. R. Rudder and D. R. Bach, *J. Opt. Soc. Am.* **58**, 1260 (1968); P. Gill and D. W. O. Heddle, *ibid.* **53**, 847 (1963); W. K. Bischel, D. J. Banford, and L. E. Jusinski, *Appl. Opt.* **25**, 1215 (1986).
- <sup>25</sup>D. F. Plusquellic, O. Votava, and D. J. Nesbitt (manuscript in preparation).
- <sup>26</sup>R. Lascola and D. J. Nesbitt, *J. Chem. Phys.* **95**, 7917 (1991); D. J. Nesbitt and R. Lascola, *ibid.* **97**, 8096 (1992).
- <sup>27</sup>H. M. Crosswhite and G. H. Dieke, *J. Quant. Spectrosc. Radiat. Transfer* **2**, 97 (1962).
- <sup>28</sup>I. L. Chidsey and D. R. Crosley, *J. Quant. Spectrosc. Radiat. Transfer* **23**, 187 (1980).
- <sup>29</sup>W. L. Dimpfl and J. L. Kinsey, *J. Quant. Spectrosc. Radiat. Transfer* **21**, 233 (1979).
- <sup>30</sup>J. A. Silver, W. L. Dimpfl, J. H. Brophy, and J. L. Kinsey, *J. Chem. Phys.* **65**, 1811 (1976).
- <sup>31</sup>K. Shimoda, in *High Resolution Laser Spectroscopy*, edited by K. Shimoda (Berlin Springer Verlag, New York, 1976).
- <sup>32</sup>W. D. Gwinn, B. E. Turner, W. M. Goss, and G. L. Blackman, *Astrophys. J.* **179**, 789 (1973); M. Bertojo, A. C. Cheung, and C. H. Townes, *ibid.* **208**, 914 (1976).
- <sup>33</sup>J. M. Brown and J. E. Schubert, *J. Mol. Spectrosc.* **95**, 194 (1982).
- <sup>34</sup>N. Shafer, S. Satyapal, and R. Bersohn, *J. Chem. Phys.* **90**, 6807 (1989).
- <sup>35</sup>J. R. Reimers and R. O. Watts, *Mol. Phys.* **52**, 357 (1984); D. F. Coker and R. O. Watts, *J. Phys. Chem.* **91**, 2513 (1987); D. F. Coker, R. E. Miller, and R. O. Watts, *J. Chem. Phys.* **82**, 3554 (1985).
- <sup>36</sup>M. S. Child, in *Semiclassical Mechanics with Molecular Applications* (Clarendon, Oxford, 1991); W. H. Miller, *J. Chem. Phys.* **48**, 464 (1968).
- <sup>37</sup>J. M. Flaud and C. Camy-Peyret, *Mol. Phys.* **26**, 811 (1973); *J. Mol. Spectrosc.* **51**, 142 (1974); F. M. Dalby and H. J. Nielsen, *J. Chem. Phys.* **25**, 934 (1956); C. Camy-Peyret and J. M. Flaud, *Spectrochim. Acta* **29A**, 1711 (1973); *J. Mol. Spectrosc.* **59**, 327 (1976); G. A. Khachkuruzor, *Opt. Spectrosc. Cong.* **4**, 294 (1959); W. S. Benedict, A. M. Bass, and E. K. Plyler, *J. Res. Natl. Bur. Std.* **52**, 161 (1954); R. Mecke, *Z. Phys.* **81**, 313,445,465 (1933).
- <sup>38</sup>O. L. Polyansky, P. Jensen, and J. Tennyson, *J. Chem. Phys.* **101**, 7651 (1994).
- <sup>39</sup>R. J. Sension, R. J. Brudzynski, and B. S. Hudson, *Phys. Rev. Lett.* **61**, 694 (1988).
- <sup>40</sup>J. Zhang and D. G. Imre, *J. Chem. Phys.* **90**, 1666 (1989).
- <sup>41</sup>S. Hennig, V. Engel, R. Schinke, and V. Staemmler, *Chem. Phys. Lett.* **149**, 455 (1988); V. Engel, V. Staemmler, R. L. Vander Wal, F. F. Crim, R. J. Sension, B. Hudson, P. Andresen, S. Hennig, K. Weide, and R. Schinke, *J. Phys. Chem.* **96**, 3201 (1992).
- <sup>42</sup>K. Watanabe and M. Zelikoff, *J. Opt. Soc. Am.* **43**, 753 (1953); R. D. Hudson, *Rev. Geophys. Space Phys.* **9**, 305 (1971); A. H. Laufer and J. R. McNesby, *Can. J. Chem.* **43**, 3487 (1965).
- <sup>43</sup>R. J. Fallon, I. Tobias, and J. T. Vanderslice, *J. Chem. Phys.* **34**, 167 (1961).